Low Voltage Operating Field Effect Transistors with Composite In_2O_3–ZnO–$ZnGa_2O_4$ Nanofiber Network as Active Channel Layer

Seung-Hoon Choi,[†] Bong-Hoon Jang,[‡] Jin-Seong Park,[§] Renaud Demadrille,[⊥] Harry L. Tuller,[∥] and Il-Doo Kim[‡,*]

[†]Optoelectronic Materials Center, Korea Institute of Science and Technology, P.O. Box 131, Cheongryang, Seoul, Republic of Korea, [‡]Department of Materials Science and Engineering, Korea Advanced Institute of Science and Technology, Daejeon 305-701, Republic of Korea, [§]Division of Materials Science and Engineering, Hanyang University, 222 Wangsimni-ro Seongdong-gu, Seoul, 133-719, Republic of Korea, [⊥]INAC/SPrAM (UMR 5819 CEA-CNRS-Univ. J. Fourier-Grenoble 1), Laboratoire d'Electronique Moléculaire Organique et Hybride, 17 Rue des Martyrs, 38054 Grenoble Cedex 9, France, and [∥]Department of Materials Science and Engineering, Massachusetts Institute of Technology, Cambridge, Massachusetts 02139 United States

ABSTRACT Field effect transistors (FETs), incorporating metal-oxide nanofibers as the active conductive channel, have the potential for driving the widespread application of nanowire or nanofiber FETs-based electronics. Here we report on low voltage FETs with integrated electrospun In_2O_3–ZnO–$ZnGa_2O_4$ composite fiber channel layers and high-K dielectric $(MgO)_{0.3}$-$(Bi_{1.5}Zn_{1.0}Nb_{1.5}O_7)_{0.7}$ gate insulator and compare their performance against FETs utilizing conductive single phase, polycrystalline ZnO or In_2O_3 channel layers. The polycrystalline In_2O_3–ZnO–$ZnGa_2O_4$ composite fibers provide superior performance with high field effect mobility (~7.04 $cm^2V^{-1}s^{-1}$), low subthreshold swing (390 mV/dec), and low threshold voltage (1.0 V) combined with excellent saturation, likely resulting from the effective blocking of high current-flow through the In_2O_3 and ZnO nanocrystallites by the insulating spinel $ZnGa_2O_4$ phase. The microstructural evolution of the individual In_2O_3, ZnO, and $ZnGa_2O_4$ phases in composite fibers is clearly observed by high resolution TEM. A systematic examination of channel area coverage, ranging from single fiber to over 90% coverage, demonstrates that low coverage results in relatively low current outputs and reduced reproducibility which we attribute to the difficulty in positioning fibers and fiber length control. On the other hand, those with ~80% coverage exhibited high field effect mobility, high on/off current ratios (>10^5), and negligible hysteresis following 15 sweep voltage cycles. A special feature of this work is the application of the FETs to modulate the properties of complex polycrystalline nanocomposite channels.

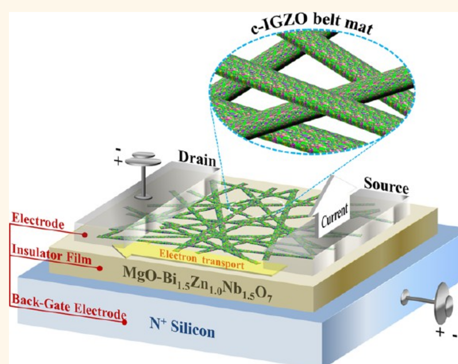

KEYWORDS: electrospinning · nanofibers · In–Ga–Zn–O composite-oxide · semiconducting channel · field effect transistors · high-K gate insulator · low voltage operation

Field effect transistors (FETs), employing high carrier mobility one-dimensional (1D) semiconducting nanowires (NWs) or nanofibers, are of great interest for integration within future nanoelectronic devices, given their unique crystalline structures, large surface to volume ratios and distinctive transport characteristics.[1−4] In particular, high density, transparent and flexible FET devices, utilizing nanowires/fibers, especially optimized for memory and logic devices,[5−7] chemical sensors,[8−10] bioprobes,[11−13] or active matrix organic light emitting diodes (AMOLED)[14] have been successfully demonstrated. However, the yield of such devices remains low, with properties exhibiting large standard deviations, resulting from the 'pick-and-place',[2,3,15] nanoimprinting,[16] and flow-directed alignment methods[17] typically utilized in their production. Multiple nanowire/fiber networks, instead of single nanowires/fibers, promise more reliable FET devices and higher device yield.[18]

In most highly integrated, high-density device applications, elemental materials such as Si,[19] Ge,[20] and graphene,[21] or binary compounds such as CdS,[2] ZnO,[22−24]

* Address correspondence to idkim@kaist.ac.kr.

Received for review November 6, 2013 and accepted February 1, 2014.

Published online February 01, 2014
10.1021/nn405769j

© 2014 American Chemical Society

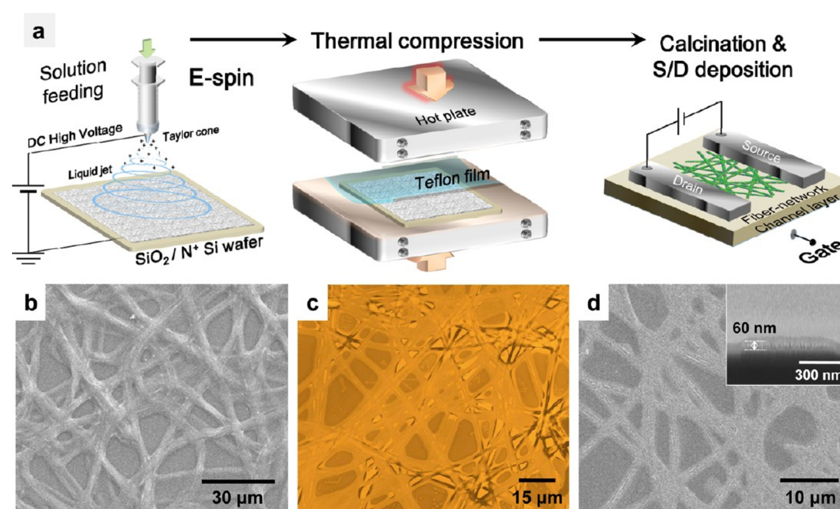

Figure 1. (a) Schematic illustration of the processing steps used in fabricating polycrystalline In_2O_3−ZnO−$ZnGa_2O_4$ fiber-network FETs; (b) FE-SEM image of as-spun (In−Ga−Zn precursor)/PVAc composite fibers on SiO_2/Si substrate; (c) confocal microscopic image of (In−Ga−Zn precursor)/PVAc composite fibers after thermo-compression at 120 °C for 100 s; (d) FE-SEM image of In_2O_3−ZnO−$ZnGa_2O_4$ fiber-network calcined at 560 °C for 1 h under O_2 ambient (inset shows cross-sectional image of calcined single fiber).

In_2O_3,[25,26] and CuO[27] have been investigated as the FET channel material. Here we report a new type of FET device, prepared by an electrospinning process, and characterized by (1) a composite (In_2O_3)−(ZnO)−($ZnGa_2O_4$) fiber network as the conducting channel, (2) improved adhesion and alignment of the fibers to the gate oxide, and the (3) integration of a high-K gate dielectric. This, as demonstrated below, leads to devices with high field effect mobility, low threshold voltage and subthreshold swing, and negligible hysteresis. Furthermore, it offers a unique opportunity to examine how the field effect can be used to modulate the properties of more complex polycrystalline composites.

Electrospinning has been widely used to produce long continuous organic or inorganic semiconducting fibers.[18,28] Electrospun semiconductor nanofibers offer flexibility in design of the channel material, efficient modulation of carriers within the channel, and ease of scale-up for large area devices. Recent efforts have demonstrated a practical means for fabricating nanofibers as uniaxially aligned arrays, enabling the realization of device architectures minimizing carrier scattering.[29] Low voltage operating FETs have been reported utilizing electrospun conjugated polymer fibers and ion gel gate dielectrics.[18] Electrospun metal oxide nanofibers offer a combination of interesting characteristics, not shared by organic and/or covalent semiconducting materials, including high carrier mobility, exceptional chemical and thermal stability and gas sensitivity. Recently Wu *et al.* fabricated FETs by direct assembly of metal oxide nanofibers composed of ZnO[30] or CuO.[31] Since the polycrystalline oxide nanofibers are synthesized *via* a high temperature calcination process to remove the polymer matrix, uneven surface morphology and low density are often observed, detrimental to FETs properties. Poor interfacial adhesion between the metal oxide nanofibers and gate oxide and difficulty in making reliable electrical contacts to the oxide fibers further increase the difficulties in achieving adequate and reproducible field effect performance. In this study, In_2O_3−ZnO−$ZnGa_2O_4$ composite fibers, containing insulating $ZnGa_2O_4$ nanocrystallites,[32] are introduced, leading to superior field effect performance. The key issues regarding reproducible device performance and interfacial contact between the active channel and the gate oxide layers are addressed by introduction of a hot-pressing step into the device fabrication process.[33,34] The FETs, utilizing In_2O_3−ZnO−$ZnGa_2O_4$ fiber-channel layers, combined with high-K dielectric $(MgO)_{0.3}$-$(Bi_{1.5}Zn_{1.0}Nb_{1.5}O_7)_{0.7}$ composite gate insulators, are demonstrated to exhibit high field effect mobility, low subthreshold swing, low threshold voltage, and negligible hysteresis characteristics.

RESULTS AND DISCUSSION

A schematic illustration of the process used in fabricating polycrystalline In_2O_3−ZnO−$ZnGa_2O_4$ fiber-network FETs is shown in Figure 1a. Figure 1b−d shows FE-SEM and confocal microscopy images of the In_2O_3−ZnO−$ZnGa_2O_4$ channel layers during each process step. In the first step, (In−Ga−Zn precursor)/PVAc (polyvinyl acetate) composite fibers are electrospun onto SiO_2 (100 nm)/Si substrates. Usually, randomly oriented fiber networks are obtained in conventional electrospinning as a result of the bending instability of the polymer/metal-salt composite fiber ejected from the single nozzle (Figure 1b). The metal halide in the polyvinyl acetate matrix fiber is highly hydrophilic and

immediately absorbs water from the atmosphere. This results in the deposited composite fibers exhibiting a quasi-elliptical structure, with fiber diameters ranging from 1 to 2 μm, formed by the partial "welding" between fibers and substrate. As described previously,[33,34] when the as-spun metal precursor/polymer composite fiber is calcined at elevated temperatures (above 350 °C), the fiber mats that are formed, exhibit poor adhesion and thus tend to peel from the substrate. To overcome this detrimental effect which could lead to fatal flaws in device fabrication, a thermo-compression step is introduced to induce partial and/or full melting of the (In–Ga–Zn precursor)/PVAc composite fibers prior to calcination. Following the thermal compression step, an interconnected morphology of the (In–Ga–Zn precursor)/PVAc composite belt-type sheets is obtained (Figure 1c). Subsequent calcination at 560 °C for 1 h results in a stable adherent fiber network structure composed of the crystalline metal oxides with a thickness of 60 nm (Figure 1d). Because charge carrier density is strongly affected by channel thickness, it is important to maintain it close to the optimum thickness, usually in the range between 30 and 100 nm.[35] In this regard, the quasi-elliptical shape, induced by the hot-pressing step, is highly desirable for good FET performance, given improved field distribution.

To examine the crystalline structure of the electrospun composite fibers as a function of different calcinations temperatures, an XRD analysis of the fiber mats, calcined from 560 to 1100 °C, was carried out in the 2θ range between 20° and 80°. Separate single phase In_2O_3, ZnO, and $ZnGa_2O_4$ fiber mats were also prepared as reference specimens and calcined under the same conditions as those of the In_2O_3–ZnO–$ZnGa_2O_4$ composite fibers for comparison of phase evolution (Figure 2a–c). When the calcination temperature reached 560 °C, the composite fibers exhibited characteristic diffraction peaks of In_2O_3, ZnO, and $ZnGa_2O_4$. These included the cubic bixbyte In_2O_3 phase characterized by primary (211), (222) and (433) peaks (corresponding to PDF 65-3170), wurtzite ZnO characterized by primary (100), (002), and (101) peaks (corresponding to PDF 65-3411) and crystalline $ZnGa_2O_4$, characterized by diffraction peaks at 2θ = 30.4°, 35.7°, 37.3°, and 43.4° assigned to the (220), (311), (222), and (400) planes (corresponding to PDF 38-1240) (Figure 2d). Zinc gallate ($ZnGa_2O_4$) exhibits the normal spinel crystal structure in which the Ga^{3+} ion occupies the octahedral site and the Zn^{2+} ion occupies the tetrahedral site. These results indicate that nanocrystallites of the In_2O_3, ZnO and $ZnGa_2O_4$ phases coexist in the composite fiber mats. Individual phases are well matched to the reference specimens of electrospun In_2O_3, ZnO, and $ZnGa_2O_4$ fibers (Figure 2a–c). $ZnGa_2O_4$ is electrically insulating, as demonstrated below, consistent with its large optical

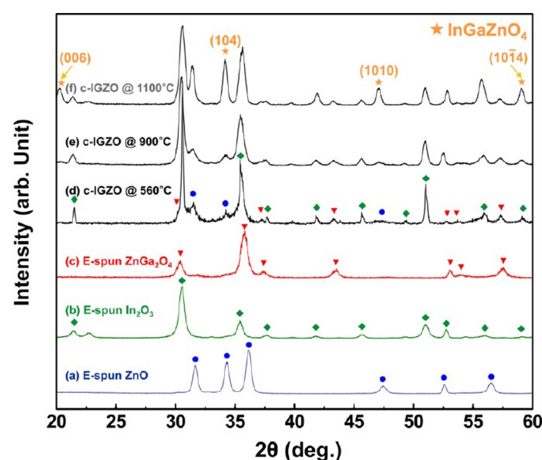

Figure 2. X-ray diffraction patterns of electrospun (a) ZnO, (b) In_2O_3, (c) $ZnGa_2O_4$ fiber mats calcined at 560 °C for 1 h and electrospun In_2O_3–ZnO–$ZnGa_2O_4$ composite fiber mats calcined at (d) 560 °C for 1 h, (e) 900 °C for 1 h, and (f) 1100 °C for 1 h.

band gap of ~5 eV.[32] One thus expects that current flow would be suppressed along the crystallite domains of $ZnGa_2O_4$ within the In_2O_3–ZnO–$ZnGa_2O_4$ multiphase channel fibers. When the calcination temperature exceeds 900 °C, the above phases react to form the $InGaZnO_4$ phase, exhibiting the diffraction peaks of the (006), (104), (1010), and (10$\bar{1}$4) planes found at 2θ = 20.3°, 34.2°, 47.1°, and 59.0°. The evolution of the various phases upon heating to 560 °C and above can be followed in Figure 2d–f.

Figure 3 shows representative TEM micrographs of a number of In_2O_3–ZnO–$ZnGa_2O_4$ composite fibers following calcination at 560 °C under O_2 ambient for 1 h. In_2O_3–ZnO–$ZnGa_2O_4$ fibers showed a regular nonwoven structure. The low magnification TEM images in Figure 3a,b show that the composite fibers are composed of nanocrystallites with size distributions of approximately 15–35 nm within fibers with diameters ranging from *ca.* 85 to 170 nm. The polycrystalline nature of the In_2O_3–ZnO–$ZnGa_2O_4$ composite fibers is clearly observed at higher magnifications (Figure 3c). The individual lattice images of interconnected nanocrystals obtained at even higher magnifications show lattice fringes that can be identified with crystallographic planes of the cubic bixbyte In_2O_3, wurtzite ZnO and spinel $ZnGa_2O_4$ phases, respectively. Figure 3d–f shows a magnified high-resolution TEM image of the colored areas in the In_2O_3–ZnO–$ZnGa_2O_4$ fiber region (Figure 3c). The green- and red-colored areas highlighted in Figure 3c show the lattice fringes having interplanar spacing of 5.00 and 4.93 Å with an angle of 90.3° between them, corresponding to cubic In_2O_3 (020) and (200) planes. The $ZnGa_2O_4$ region, displaying lattice fringes of 3.01, 2.56, and 4.86 Å, is oriented at angles of 32.5° and 59.4°, representing the (2$\bar{2}$0), (1$\bar{3}$1), and ($\bar{1}\bar{1}$1) planes,

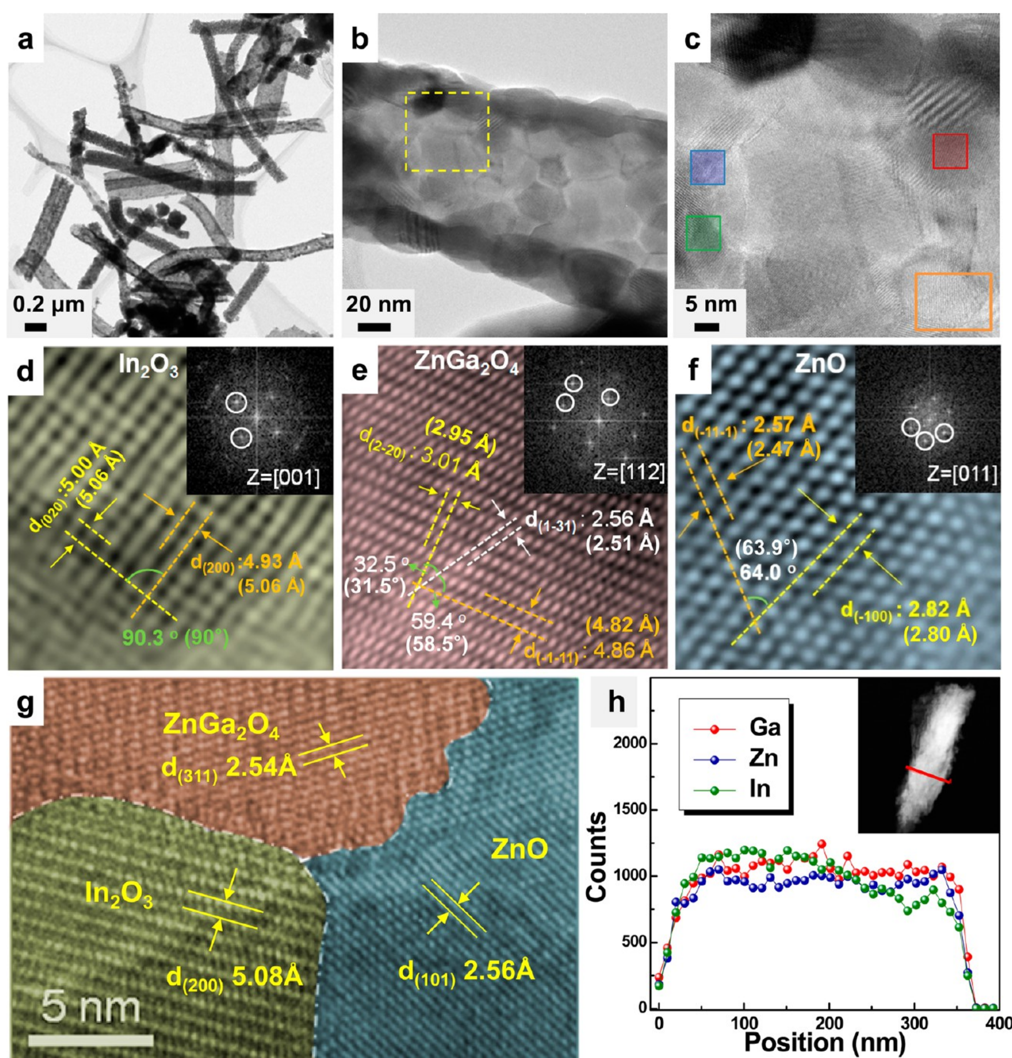

Figure 3. (a) TEM micrograph of a group of In_2O_3−ZnO−$ZnGa_2O_4$ composite fibers; (b) TEM image of a single composite fiber; (c) HR-TEM image of the dotted area selected in (b); enlarged high-magnification image of (d) green-; (e) red-; (f) blue-; (g) orange-colored areas highlighted in (c); (h) scanning TEM and EDS elemental mapping of In, Ga, and Zn elements.

respectively. The blue-colored area, assigned to ZnO, represents interplanar distances of 2.53 and 2.82 Å with an angle of 64° between the respective planes corresponding to $(01\bar{1})$ and $(\bar{1}00)$ planes. These measured values are in good agreement with the theoretical values for In_2O_3, ZnO and $ZnGa_2O_4$. A representative image of the random network of spatially interconnected In_2O_3, ZnO or $ZnGa_2O_4$ nanocrystals, formed after calcination at 560 °C for 1 h, is shown in Figure 3g (orange box highlighted in Figure 3c). A compositional line profile, obtained by Energy Dispersive Spectroscopy (EDS) analysis, reveals that the In/Ga/Zn chemical composition ratio of In_2O_3−ZnO−$ZnGa_2O_4$ fiber is approximately 1:1:1 (Figure 3h). The stoichiometric ratios of cations, originally in the precursor solution, were thus maintained in the composite oxide fibers following high temperature calcination.

To investigate the role of individual constituents in terms of charge transport, *i.e.*, In_2O_3, ZnO, and $ZnGa_2O_4$, comprising the In_2O_3−ZnO−$ZnGa_2O_4$ composite fibers, two-probe *I*−*V* measurements were conducted on 4 different fiber mats (In_2O_3, ZnO, $ZnGa_2O_4$, and In_2O_3−ZnO−$ZnGa_2O_4$ composite), which are all calcined at 560 °C under O_2 ambient for 1 h (Supporting Information Figure S1). In previous studies, In_2O_3, ZnO or their composite thin films fabricated from sol−gel method have exhibited high carrier concentration ($\sim 3 \times 10^{20}$ cm^{-3}) and high electrical conductivity ($\sim 6.7 \times 10^2$ S cm^{-1}).[36,37] However, the electrical conductivity of the electrospun In_2O_3 and ZnO fiber mats exhibited lower values of 7.9×10^{-2} and 8.8×10^{-4} S cm^{-1}, respectively, approximately 4 or 5 orders of magnitude lower than those of sol−gel processed In_2O_3 and ZnO thin films. The lower electrical conductivities of the nanostructured polycrystalline metal oxide fibers might be attributed to high interface contact resistance between individual polycrystalline metal oxide fibers associated with low film density.[37] As noted above, the $ZnGa_2O_4$ fiber mats exhibit very low room temperature conductivity

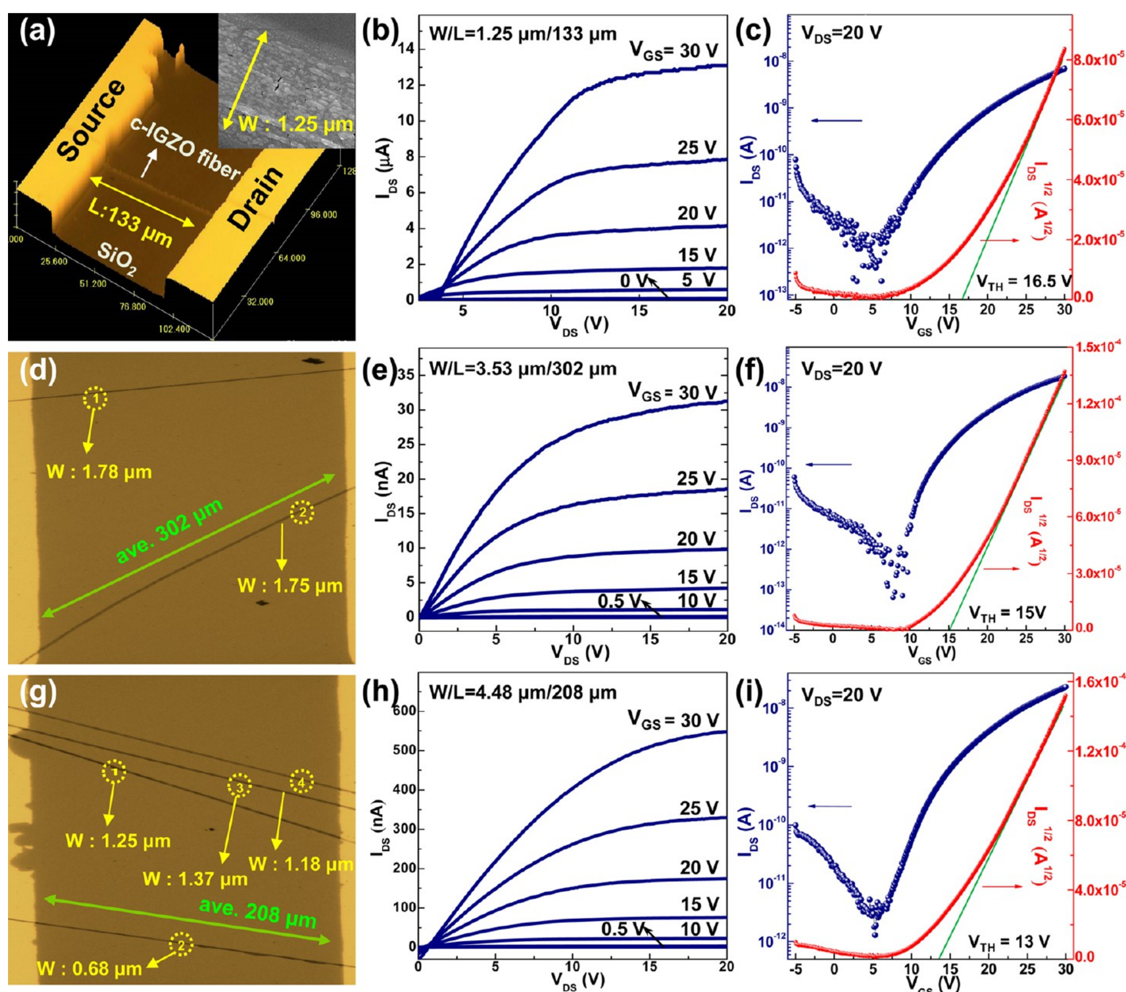

Figure 4. (a) Confocal microscopy image of the channel comprising a single In_2O_3−ZnO−$ZnGa_2O_4$ fiber-FET (inset shows SEM image of composite fiber); (b) output and (c) transfer characteristics of a single composite fiber-FET; (d) confocal microscopy image of FETs with two composite fibers; (e) output and (f) transfer characteristics of a two composite fiber-FET; (g) confocal microscopy image of the channel containing a four composite fiber-FET; (h) output and (i) transfer characteristics of a four composite fiber-FET (see Supporting Information, Table S2).

measured in this study to be 9.0 × 10^{-8} S cm^{-1}. The measured conductivity (7.5 × 10^{-4} S cm^{-1}) of the In_2O_3−ZnO−$ZnGa_2O_4$ composite fibers therefore falls intermediate between the most highly conducting In_2O_3 and the highly insulating $ZnGa_2O_4$ phases. It is well-known that the mobility of electrons, as well as current flow, may be considerably suppressed by the scattering and blocking of electrons at grain and phase boundaries within a composite system, particularly one including insulating phases. The electron transfer from either ZnO or In_2O_3 to $ZnGa_2O_4$ phase is considerably interrupted given the very low charge carrier density in $ZnGa_2O_4$.

To further investigate the electrical transport characteristics of In_2O_3−ZnO−$ZnGa_2O_4$ composite fibers, FETs, with thermo-compressed and calcined fiber-based channel layers, were fabricated. Electronic transport properties were examined using ZnO, In_2O_3 and In_2O_3−ZnO−$ZnGa_2O_4$ fiber-based FETs, offering the ability to isolate the contributions of the individual phases. The *I*−*V* characteristics of the FETs with In_2O_3−ZnO−$ZnGa_2O_4$ fibers were measured with a varying number of nanofiber channels (1, 2, and 4 fibers) situated between the Al source and drain electrodes. Figure 4a shows a confocal microscopy image of the channel containing a single In_2O_3−ZnO−$ZnGa_2O_4$ fiber. The drain-to-source current (I_{DS}) characteristics are shown in Figure 4b as a function of drain-to-source voltage (V_{DS}) at various gate-to-source voltages (V_{GS}). Figure 4c shows the transfer characteristics of the single In_2O_3−ZnO−$ZnGa_2O_4$ fiber-FET. The device exhibits reasonable gate modulation, clear pinch off and excellent saturation of the drain current with enhancement mode operation. We speculate that these results from suppressed electron transfer through the In_2O_3 and ZnO grains by the insulating $ZnGa_2O_4$ nanocrystallites, even under high electric field. On the contrary, the output characteristics of single ZnO fiber-FETs did not exhibit current saturation even at higher V_{DS} and V_{GS} (>20 V) (Supporting Information Figure S4).

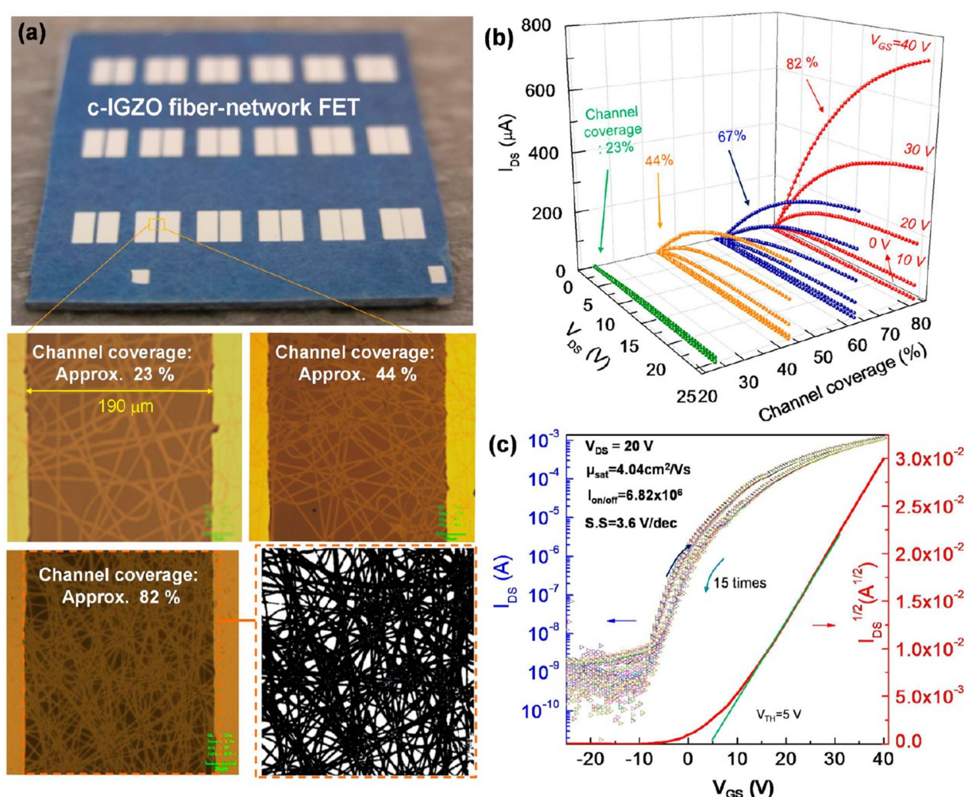

Figure 5. (a) Photographic image of In_2O_3−ZnO−$ZnGa_2O_4$ fiber based FET arrays with channel length of 190 μm; corresponding confocal microscopy images captured with different coverage of 23, 44, 67, and 82%; (b) output characteristics ($I_{DS} - V_{DS}$) with four different channel coverages of 23, 44, 67, and 82%; (c) transfer characteristics of composite fiber network-FET having 82% channel coverage with gate voltage swept from −25 to 40 V at a fixed V_{DS} of 20 V.

The poor saturation characteristics of the single ZnO fiber-FET imply that free electrons are not entirely depleted at the interface between the ZnO channel layer and the SiO_2 gate insulator, hinting that higher electric fields between drain and source are needed for current saturation.

The maximum on-current is observed to depend strongly on the number of fibers making up the FET channel, as illustrated in Figure 4b,e,h. for devices with one, two, and four fibers. The transfer curves, measured by sweeping V_{GS} from −5 to +30 V at V_{DS} = 20 V are shown in Figures 4c,f,i, with all of the FETs containing one, two, and four In_2O_3−ZnO−$ZnGa_2O_4$ fibers exhibiting good operating performance with on−off ratio ($I_{on/off}$) of 3.6 × 10^4, 5.3 × 10^4, and 1.9 × 10^4, respectively. The field effect mobilities (μ_{eff}) in the saturation region were extracted from the relationship $(I_{DS})^{1/2} = (W/2LC_i\mu)^{1/2}(V_{GS} - V_{th})$, where C_i is the gate dielectric capacitance per unit area and W and L represent the width and length of the In_2O_3−ZnO−$ZnGa_2O_4$ fiber channels, respectively. The threshold voltage (V_{th}) can be estimated by extrapolation of the linear portion of $(I_{DS})^{1/2}$ *vs* V_{GS}. The width of the devices was extracted from the sum of the lengths of all fibers bridging the source and drain electrodes. The extracted μ_{eff} values for the FETs with one, two, and four fiber layers were 0.22, 0.39, and 0.27 $cm^2V^{-1}s^{-1}$, respectively. The threshold voltage decreases slightly from 16.5 to 13 V as the fiber number is increased due to the increase in the number of free electrons associated with the increasingly wide electron pathway. This indicates that the electrical properties can be controlled by adjusting the number of fibers. However, in terms of operational reliability, the electrical properties of the FETs are strongly dependent on the channel area ($W \times L$). These few numbers of active fibers per device provide relatively low current outputs, poor uniformity and low reproducibility due to the difficulty in positioning the fibers and controlling their lengths.

This suggests that FETs with few numbers of electrospun fibers may not be suitable for practical device fabrication and large-scale integration. To address this issue, a two-dimensional (2D) channel network design, with good contact properties between channels and dielectric layers, was introduced. Fiber network films with various channel coverage and density were prepared by varying the fiber deposition time during the electrospinning process. Channel coverage was further carefully controlled by adjusting the electrospinning conditions, *i.e.*, the flow rate of precursor solution, collection time, distance between nozzle and collector and thermal compression conditions such as compression pressure, hot plate temperature and compression time. Figure 5a shows a confocal microscopy image of

an array of $In_2O_3-ZnO-ZnGa_2O_4$ fiber network-FETs with channel length of 190 μm with varying area density coverage of 23, 44, 67 and 82%. Figure 5b shows the output characteristics ($I_{DS} - V_{DS}$) for the FETs with the four different channel coverages of 23, 44, 67 and 82%.

The $In_2O_3-ZnO-ZnGa_2O_4$ channels with very thin belt (60 nm thickness) structures, formed by hot-pressing and followed by high temperature calcination, exhibit a random network on the substrate. Fiber coverage is defined as the ratio of the area covered by the electrospun $In_2O_3-ZnO-ZnGa_2O_4$ fiber network to that of the physical channel area ($W \times L$). The 4 different FETs exhibit good operating performance with excellent current saturation behavior even at high gate voltage (>30 V) and on/off ratios ($I_{on/off}$) of over 10^5. Although the current saturation properties slightly deteriorate with increasing fiber coverage, the drain current increases significantly from 30 to 700 μA with increasing channel coverage from 23% to 82%. The maximum on-current and $I_{on/off}$ values extracted from the transfer curves of FETs as a function of channel coverage are presented in Supporting Information Figure S5. One observes the maximum on-current and $I_{on/off}$ improve as the fiber network channel coverage is increased from 23 to 82%. The off-current is not substantially changed with variation of channel coverage. The $I_{on/off}$ values were 1.05×10^5, 1.1×10^5, 1.9×10^6, and 6.82×10^6 at V_{DS} = 20 V, for FETs with 23, 44, 67, and 82% coverage, respectively. For FET devices with polycrystalline channels, an increase in the number of channel stripes results in an enhancement of the on-state current given that better gate control capability induces lower grain boundary potential barriers.[38] However, when channel coverage exceeded approximately 90%, the device characteristics were observed to sharply deteriorate. While the network channel layer showed a very high maximum on-current of 1.68 mA, it exhibited poor saturation behavior and low $I_{on/off}$ of 3.9×10^3 at a V_{DS} = 20 V. The deteriorated electrical properties, such as higher off-current, may have resulted from an increase in fiber network channel layer thickness. In addition, a continuous fiber stack may result in a morphological change from a two-dimensional (2D) belt network film to a three-dimensional (3D) network architecture due to the overlapping of many individual fibers, resulting in an uneven channel thickness. These morphologies may significantly impact the character of the interface between semiconductor and gate insulator, and thereby device modulation efficacy. On the basis of the above observations, the optimum $In_2O_3-ZnO-ZnGa_2O_4$ fiber network channel coverage was found to be 80 ± 5% in terms of the trade-off between highest on/off ratio and maximum on-state current.

The transfer characteristics were investigated using $In_2O_3-ZnO-ZnGa_2O_4$ fiber network-FETs having 82% channel coverage. In these measurements, the gate voltage was swept from −25 to 40 V at a fixed V_{DS} of 20 V which is in the saturation region (Figure 5c). The measured field effect mobility (μ_{eff}) and threshold voltage (V_{th}) were 4.04 $cm^2/(V\ s)$ and 5 V, respectively. Moreover, little hysteresis behavior was observed in air when sweeping V_{GS} in the forward and reverse directions, indicating that these devices remain stable in an atmosphere ambient. This suggests that only few active charge trap sites exist between the semiconducting $In_2O_3-ZnO-ZnGa_2O_4$ fiber network and the SiO_2 gate insulator. According to a previous study, applying electrostatic simulations to the electric-field distribution in the cross section of a nanowire FET with various nanowire coverages, the gate capacitances of nanowire FETs (130 nm thick SiO_2 dielectric layer), with above 60% nanowire coverage in the channel area, exhibit similar values to a continuous planar thin-film of the same material and thickness.[15] Therefore, the effects of increasing transconductance (g_m) and decreasing effective gate capacitance per wire (C_w) nearly completely counterbalance each other above a certain nanowire coverage. Thus the performance of devices no longer improves with increased nanowire coverage. On the basis of these observations, we can speculate that $In_2O_3-ZnO-ZnGa_2O_4$ fiber network-FETs with 82% channel coverage at the SiO_2 dielectric layer (100 nm) should behave similarly to a continuous planar thin film of the same material and thickness. Assuming 100% fiber coverage on the channel area, one calculates the field effect mobility (μ_{eff}) from the parallel-plate model. Following this approach, an average μ_{eff} equal to 2.04 $cm^2/(V\ s)$ was calculated from the slope of the $(I_{DS})^{1/2}$ *vs* V_{GS} curves obtained from more than 25 FET devices with 82% channel coverage. On the other hand, similar channel coverage FET devices composed of In_2O_3 (75%) or ZnO (78%) fiber networks prepared by the same electrospinning conditions and FET fabrication process (Supporting Information Figure S6) have a largely negative V_{th} and poor saturation behavior at high V_{DS}, suggesting that the channel-layers were too conductive as formed, presumably owing to the tendency of In_2O_3 and ZnO to form oxygen vacancies.[35] The $In_2O_3-ZnO-ZnGa_2O_4$ fiber network-FETs using a SiO_2 gate insulator, on the other hand, exhibited satisfactory performance, *i.e.*, high field effect mobility (4.04 $cm^2/(V\ s)$), high on/off ratio (>10^5), negligible hysteresis behavior even after 15 sweep cycles, and reasonable threshold voltage (5 V).

To further improve the performances of FET devices utilizing the $In_2O_3-ZnO-ZnGa_2O_4$ fiber network channel, high-K $(MgO)_{0.3}$-$(Bi_{1.5}Zn_{1.0}Nb_{1.5}O_7)_{0.7}$ gate insulator thin films, prepared by rf-sputtering, were introduced enabling low voltage operation. In previous work, the leakage current characteristics of high-K $Bi_{1.5}Zn_{1.0}Nb_{1.5}O_7$ (BZN) gate insulators were demonstrated to be markedly improved by the addition to the

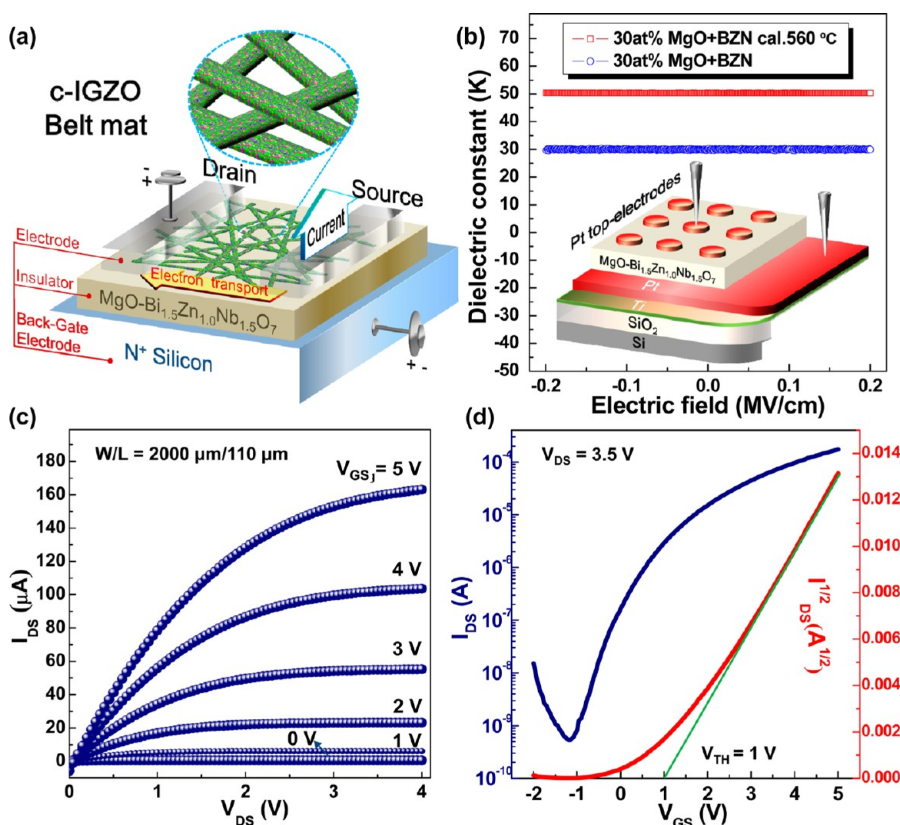

Figure 6. (a) Schematic illustration of the composite fiber network-FET with high-k $(MgO)_{0.3}$-$(Bi_{1.5}Zn_{1.0}Nb_{1.5}O_7)_{0.7}$ gate dielectric layer; (b) the dielectric constant *vs* electric field characteristics of as-deposited and calcined $(MgO)_{0.3}$-$(Bi_{1.5}Zn_{1.0}Nb_{1.5}O_7)_{0.7}$ thin films with thickness of 250 nm; (c) output and (d) transfer characteristics of composite fiber network-FETs with $(MgO)_{0.3}$-$(Bi_{1.5}Zn_{1.0}Nb_{1.5}O_7)_{0.7}$ gate insulator.

BZN of 30 atomic % MgO, a large band gap (7.8 eV) insulator with high breakdown strength.[39]

Figure 6a illustrates a schematic of the fabricated In_2O_3−ZnO−$ZnGa_2O_4$ fiber (approximately 81% channel coverage) network-FET with high-K $(MgO)_{0.3}$-$(Bi_{1.5}Zn_{1.0}Nb_{1.5}O_7)_{0.7}$ gate dielectric layer calcined at 560 °C for 1 h. The dielectric constant-electric field characteristics of the as-deposited and calcined $(MgO)_{0.3}$-$(Bi_{1.5}Zn_{1.0}Nb_{1.5}O_7)_{0.7}$ thin films, with thickness of 250 nm, were investigated (Figure 6b). A dielectric constant of 51 was calculated for the $(MgO)_{0.3}$-$(Bi_{1.5}Zn_{1.0}Nb_{1.5}O_7)_{0.7}$ thin film, using the definition of capacitance given by $C=\varepsilon_0\varepsilon_r/d$ (where C is the capacitance per area, ε_0 is the permittivity of vacuum, and d is the thin-film thickness). This value was approximately 1.7 times higher than that (ε_r = 30) of the as-deposited $(MgO)_{0.3}$-$(Bi_{1.5}Zn_{1.0}Nb_{1.5}O_7)_{0.7}$ thin film without calcination treatment. The higher relative dielectric constant (51) of the calcined $(MgO)_{0.3}$-$(Bi_{1.5}Zn_{1.0}Nb_{1.5}O_7)_{0.7}$ thin film was attributed to crystallization of the $Bi_{1.5}Zn_{1.0}Nb_{1.5}O_7$ phase, as confirmed by XRD analysis[39] (Supporting Information Figure S7). The leakage current densities of the calcined $(MgO)_{0.3}$-$(Bi_{1.5}Zn_{1.0}Nb_{1.5}O_7)_{0.7}$ thin films remain within a narrow band of $\sim10^{-7}$ A/cm^2 even at 0.6 MV cm^{-1}, leading to high gate insulator breakdown strength (Supporting Information Figure S8).

Figure 6c shows the relationship between the drain-to-source current (I_{DS}) and voltage (V_{DS}) in In_2O_3−ZnO−$ZnGa_2O_4$ fiber network-FETs using the $(MgO)_{0.3}$-$(Bi_{1.5}Zn_{1.0}Nb_{1.5}O_7)_{0.7}$ gate insulator. A superior gate-modulated device characteristic with good I_{DS} saturation was observed even at 5 V operation. Figure 6d shows the transfer characteristic of In_2O_3−ZnO−$ZnGa_2O_4$ fiber network-FETs with drain-to-source voltages (V_{DS}) of 3.5 V. The gate voltage was swept from −2 to 5 V for the FETs incorporating the $(MgO)_{0.3}$-$(Bi_{1.5}Zn_{1.0}Nb_{1.5}O_7)_{0.7}$ gate insulator. The on-current and off-current of the FETs were 1.72×10^{-4} and 5.48×10^{-10} A, respectively, resulting in the on/off current ratio of 3.13×10^5. The V_{th} and μ_{eff} values calculated in the saturation region were 1.0 V and 7.04 cm^{2}V^{-1}s^{-1} and the subthreshold swing was 390 mV/dec for the FETs. The successful low-voltage operation of the In_2O_3−ZnO−$ZnGa_2O_4$ fiber network-FETs provides a milestone for realizing metal oxide nanofiber-based FETs.

CONCLUSION

In conclusion, FETs incorporating novel composite In_2O_3−ZnO−$ZnGa_2O_4$ fiber network channels fabricated *via* an electrospun metal-oxide synthesis route and combined with a high-K $(MgO)_{0.3}$-$(Bi_{1.5}Zn_{1.0}Nb_{1.5}O_7)_{0.7}$ gate insulator were demonstrated

to operate at low voltage (<5 V). The In_2O_3–ZnO–$ZnGa_2O_4$ fiber network exhibited stable semiconducting properties and superior field effect mobility (7.04 $cm^2/(V\ s)$), comparable to that (8.04 $cm^2/(V\ s)$) of amorphous $InGaZnO_4$ thin film based FETs.[40] High current flow through In_2O_3 and ZnO phases is effectively suppressed by the highly insulating $ZnGa_2O_4$ species within the composite In_2O_3–ZnO–$ZnGa_2O_4$ fiber, showing good current saturation behavior, while pure In_2O_3 and ZnO fiber network-FETs showed poor current saturation characteristics. Highly reproducible, low voltage operating composite fiber FETs show promise as being the basis of novel device platforms, with potential for application as chemical and biosensors, as demonstrated in upcoming work.

METHODS

Sample Preparation. Poly(vinyl acetate) (PVAc, M_w = 1 300 000 mol/g) was synthesized using bulk radical polymerization. Anhydrous indium(III) chloride ($InCl_3$, 99.999%), anhydrous gallium(III) chloride ($GaCl_3$, 99.999%) and zinc acetate dyhydrate ($Zn(CH_3COO)_2 \cdot 2H_2O$, 99%+) were purchased from Aldrich. Anhydrous *N*,*N*-dimethylformamide (DMF) was obtained from J.T Baker. The chemical reagents were used without further purification.

For the preparation of In_2O_3–ZnO–$ZnGa_2O_4$ composite fibers, the precursor solution for electrospinning was prepared by dissolving 1.11 g of $InCl_3$, 0.88 g of $GaCl_3$, 1.1 g of $Zn(CH_3COO)_2 \cdot 2H_2O$) and 1.5 g of PVAc in 16.5 mL of DMF. The total PVAc content in the solution was 10 wt % and the In:Zn:Ga stoichiometry was 1:1:1. To minimize formation of undesirable crystalline phases, a precursor solution with a stoichiometric ratio was carefully mixed and processed.

During the electrospinning process, the solution was injected through a stainless steel needle (25 gauge, orifice diameter = 250 μm) connected to a high-voltage DC power supply (Bertan, High-voltage power supply series 230). The solution was continuously fed through the nozzle using a syringe pump (KD scientific, 781200) at a rate of 10 μL/min. The distance between tip orifice and ground was maintained at 15 cm. High voltage (14.5 kV) was applied between the needle and the grounded collector, resulting in the emission of a continuous (In–Zn–Ga precursor)/PVAc composite fiber stream. These fibers were directly spun onto SiO_2 (100 nm, gate oxide) grown on heavily doped n-type Si wafer (back gate) substrate and thermo-compressed using preheated plates at 120 °C for 100 s using a lamination machine to provide high adhesion strength on the interface between the active channel and the gate oxide following high temperature calcination. Then the samples were calcined at 560 °C under O_2 ambient (500 sccm) for 1 h to remove the PVAc matrix by thermal decomposition and to crystallize the In_2O_3–ZnO–$ZnGa_2O_4$ fibers.

Device Fabrication. Following thermal compression and calcination, Al electrodes (200 nm) were patterned on top of the In_2O_3–ZnO–$ZnGa_2O_4$ fiber mats with the aid of a shadow mask.

The electrical conductivities (σ) of In_2O_3, ZnO, $ZnGa_2O_4$, and the In_2O_3–ZnO–$ZnGa_2O_4$ composite fiber mats prepared by electrospinning were characterized by two-probe I–V measurements (Supporting Information Figure S1). The electrical conductivity values of the 4 different fiber mats were estimated from the equation, $\sigma = l/RA$, where R is the resistance, A is the cross-sectional area, and l the distance between the electrodes. The line width of each Al electrode was 2000 μm, spaced 190 μm apart (see the schematic cross-sectional view in the inset of Figure S1).

Low voltage operating In_2O_3–ZnO–$ZnGa_2O_4$ fiber network-FETs, with $(MgO)_{0.3}$-$(Bi_{1.5}Zn_{1.0}Nb_{1.5}O_7)_{0.7}$ as gate insulator, were fabricated with the configuration: heavily doped n-type Si/$(MgO)_{0.3}$-$(Bi_{1.5}Zn_{1.0}Nb_{1.5}O_7)_{0.7}$ dielectric/In_2O_3–ZnO–$ZnGa_2O_4$ fiber network/Al (S/D) structure, as shown in Figure 6a. To deposit high-K $(MgO)_{0.3}$-$(Bi_{1.5}Zn_{1.0}Nb_{1.5}O_7)_{0.7}$ thin films, powders of said composition were prepared by a conventional mixed oxide method using reagent-grade MgO, Bi_2O_3, ZnO, and Nb_2O_5 powder. These were used to prepare 3-in. in diameter disk-type MgO-$Bi_{1.5}Zn_{1.0}Nb_{1.5}O_7$ targets from which 250 nm thick $(MgO)_{0.3}$-$(Bi_{1.5}Zn_{1.0}Nb_{1.5}O_7)_{0.7}$ films were deposited onto heavily doped n-type Si wafer by rf-magnetron sputtering with a power of 85 W, working pressure of 1.33 Pa, and an Ar/O_2 (ratio = 3:2) mixed gas of 20 sccm.

Characterization. Elemental analysis (EA) was conducted on In_2O_3–ZnO–$ZnGa_2O_4$ fibers calcined at 560 °C for 1 h. Only a negligibly small (0.30 wt %) amount of carbonaceous residue was detected, suggesting that the organic components fully volatilized during calcination. Attenuated total reflection (ATR, PIKE, mIRacle)-Fourier transform infrared spectroscopy (FTIR, Perkin-Elmer, Spectrum GX) was used to investigate the chemical state of In_2O_3–ZnO–$ZnGa_2O_4$ composite fibers during the calcination process (25–600 °C). Thermogravimetric analysis (TGA) was performed on a TG-2050 thermal analyzer system (Ta instrument, Inc.) at a heating rate of 10 °C/min under O_2 condition (flow rate: 0.5 sccm). X-ray diffraction (X-ray diffractometry, Rigaku D/MAX-RC; with Cu Kα radiation) was used to identify the crystal structure of the composite fibers. The microstructural evolution during each process step was carried out by scanning electron microscopy (SEM, JSM-6330F, JEOL) and confocal microscopy (OLYMPUS, OLS3000). A focused ion beam (FIB, Nova 600, FEI Inc.) was used to examine the cross-sectional image of the individual fibers. Transmission electron microscopy (TEM) was used to examine the microstructure of In_2O_3–ZnO–$ZnGa_2O_4$ fibers, while individual grain structures were examined by high resolution TEM (Tecnai G2, FEI Hong Kong Co., Ltd.). Ultrasonication was used to disperse the In_2O_3–ZnO–$ZnGa_2O_4$ fibers in ethanol, followed by mounting on a carbon-coated Cu grid. The electrical properties of the In_2O_3–ZnO–$ZnGa_2O_4$ fibers and leakage current characteristics of the $(MgO)_{0.3}$-$(Bi_{1.5}Zn_{1.0}Nb_{1.5}O_7)_{0.7}$ thin films were characterized by a semiconductor device analyzer (B1500A, Agilent Technologies).

A metal–insulator–metal (MIM) capacitor structure was fabricated on 100 nm thick Pt-coated Si substrate to determine the leakage current and dielectric characteristics of the $(MgO)_{0.3}$-$(Bi_{1.5}Zn_{1.0}Nb_{1.5}O_7)_{0.7}$ thin film. For the top electrode, 100 nm Pt was deposited by RF magnetron sputtering through a shadow mask on top of the 250 nm thick $(MgO)_{0.3}$-$(Bi_{1.5}Zn_{1.0}Nb_{1.5}O_7)_{0.7}$ thin film. Dielectric properties were measured over the frequency range of 1 kHz to 1 MHz with an applied voltage ranging from 0 to 15 V using a HP4192A impedance analyzer.

Conflict of Interest: The authors declare no competing financial interest.

Acknowledgment. This work was supported by the Center for Integrated Smart Sensors funded by the Ministry of Science, ICT & Future Planning as Global Frontier Project (CISS–2011–0031870).

Supporting Information Available: Experimental section; characterization; chemical structure analysis and thermal behavior of (In–Zn–Ga precursor)/PVAc composite fibers; electron transport characteristics of a single In_2O_3–ZnO–Zn_2SnO_4 composite fiber; XRD analysis and the leakage current densities of $(MgO)_{0.3}$-$(Bi_{1.5}Zn_{1.0}Nb_{1.5}O_7)_{0.7}$ thin films. This material is available free of charge *via* the Internet at http://pubs.acs.org.

REFERENCES AND NOTES

1. Huang, Y.; Duan, X.; Cui, Y.; Lauhon, L. J.; Kim, K. H.; Lieber, C. M. Logic Gates and Computation from Assembled Nanowire Building Blocks. *Science* **2001**, *294*, 1313–1317.
2. Razavieh, A.; Mehrotra, S.; Singh, N.; Klimeck, G.; Janes, D.; Appenzeller, J. Utilizing the Unique Properties of Nanowire MOSFETs for RF Applications. *Nano Lett.* **2013**, *13*, 1549–1554.
3. Chuang, S.; Gao, Q.; Kapadia, R.; Ford, A. C.; Guo, J.; Javey, A. Ballistic InAs Nanowire Transistors. *Nano Lett.* **2013**, *13*, 555–558.
4. Gao, A. R.; Lu, N.; Wang, Y. C.; Dai, P. F.; Li, T.; Gao, X. L.; Wang, Y. L.; Fan, C. H. Enhanced Sensing of Nucleic Acids with Silicon Nanowire Filed Effect Transistor Biosensors. *Nano Lett.* **2012**, *12*, 5262–5268.
5. Liao, L.; Fan, H. J.; Yan, B.; Zhang, Z.; Chen, L. L.; Li, B. S.; Xing, G. Z.; Shen, Z. X.; Wu, T.; Sun, X. W.; Wang, J.; Yu, T. Ferroelectric Transistors with Nanowire Channel: Toward Nonvolatile Memory Applications. *ACS Nano* **2009**, *3*, 700–706.
6. Yan, H.; Choe, H. S.; Nam, S. W.; Hu, Y.; Das, S.; Klemic, J. F.; Ellenbogen, J. C.; Lieber, C. M. Programmable Nanowire Cicuits for Nanoprocessors. *Nature* **2011**, *470*, 240–244.
7. Zhong, Z.; Wang, D.; Cui, Y.; Bockrath, M. W.; Lieber, C. M. Nanowire Crossbar Arrays as Address Decoders for Integrated Nanosystems. *Science* **2003**, *302*, 1377–1379.
8. Cheng, Y.; Xiong, P.; Yun, S.; Strouse, G. F.; Zheng, J. P.; Yang, R. S.; Wang, Z. L. Mechanism and Optimization of pH Sensing using SnO_2 Nanobelt Field Effect Transistors. *Nano Lett.* **2008**, *8*, 4179–4184.
9. McAlpine, M. C.; Ahmad, H.; Wang, D.; Heath, J. R. Highly Ordered Nanowire Arrays on Plastic Substrates for Ultrasensitive Flexible Chemical Sensors. *Nat. Mater.* **2007**, *6*, 379–384.
10. Fan, Z.; Lu, J. G. Gate-Refreshable Nanowire Chemical Sensors. *Appl. Phys. Lett.* **2005**, *86*, No. 123510.
11. Zhang, G. J.; Zhang, G.; Chua, J. H.; Chee, R. E.; Wong, E. H.; Agarwal, A.; Buddharaju, K. D.; Singh, N.; Gao, Z.; Balasubramanian, N. DNA sensing by Silicon Nanowire: Charge Layer Distance Dependence. *Nano Lett.* **2008**, *8*, 1066–1070.
12. Tian, B.; Cohen-Karni, T.; Qing, Q.; Duan, X.; Lieber, C. M. Three-Dimensional, Flexbile Nanoscale Field-Effect Transistors as Localized Bioprobes. *Science* **2010**, *329*, 830–834.
13. Patolsky, F.; Timko, B. P.; Yu, G.; Fang, Y.; Greytak, A. B.; Zheng, G.; Lieber, C. M. Detection, Stimulation, and Inhibition of Neuronal Signals with High-Density Nanowire Transistor Arrays. *Science* **2006**, *313*, 1100–1104.
14. Ju, S.; Li, J.; Liu, J.; Chen, P. C.; Ha, Y. G.; Ishikawa, F.; Chang, C.; Facchetti, A.; Janes, D. B.; Marks, T. J. Transparent Active Matrix Organic Light-Emitting Diode Displays Driven by Nanowire Transistor Circuitry. *Nano Lett.* **2008**, *8*, 997–1004.
15. Eric, N. D.; Qing, W.; Wei, G.; Yanbin, C.; Xiaoqing, P.; Wei, L. Fully Transparent Thin-Film Transistor Devices Based on SnO_2 Nanowires. *Nano Lett.* **2007**, *7*, 2463–2469.
16. Ahn, J. H.; Kim, H. S.; Lee, K. J.; Jeon, S.; Kang, S. J.; Sun, Y.; Nuzzo, R. G.; Rogers, J. A. Heterogeneous Three-Dimensional Electronics by Use of Printed Semiconductor Nanomaterials. *Science* **2006**, *314*, 1754–1757.
17. Huang, Y.; Duan, X.; Wei, Q.; Lieber, C. M. Directed Assembly of One-Dimensional Nanostructure into Functional Networks. *Science* **2001**, *291*, 630–633.
18. Lee, S. W.; Lee, H. J.; Choi, J. H.; Koh, W. G.; Myoung, J. M.; Hur, J. H.; Park, J. J.; Cho, J. H.; Jeong, U. Periodic Array of Polyelectrolyte-Gated Organic Transistor from Electrospun Poly(3-hexylthiophene) Nanofibers. *Nano Lett.* **2010**, *10*, 347–351.
19. Stern, E.; Klemic, J. F.; Routenberg, D. A.; Wyrembak, P. N.; Turner-Evans, D. B.; Hmilton, A. D.; LaVan, D. A.; Fahmy, T. M.; Reed, M. A. Label-free Immunodetection with CMOS-compatible Semiconducting Nanowires. *Nature* **2007**, *445*, 519–522.
20. Qin, D.; Tao, H.; Zhao, Y.; Lan, L.; Chan, K.; Cao, Y. Field Effect Transitor from Individual Trigonal Se Nanowire. *Nanotechnology* **2008**, *19*, 355201.
21. Liao, L.; Lin, Y. C.; Bao, M.; Cheng, R.; Bai, J.; Liu, Y.; Qu, Y.; Wang, K. L.; Huang, Y.; Duan, X. High-Speed Graphene Transistors with a Self-Aligned Nanowire Gate. *Nature* **2010**, *467*, 305–308.
22. Ko, S. H.; Park, I.; Pan, H.; Misra, N.; Rogers, M. S.; Grigoropoulos, C. P.; Pisano, A. P. ZnO Nanowire Network Transistor Fabrication on a Polymer Substrate by Low-temperature, All-Inorgainc Nanoparticle Solution Process. *Appl. Phys. Lett.* **2008**, *92*, No. 154102.
23. Fan, Z.; Wang, D.; Chang, P. C.; Tseng, W. Y.; Lu, J. G. ZnO Nanowire Field Effect Transistor and Oxygen Sensing Property. *Appl. Phys. Lett.* **2004**, *85*, 5923–5925.
24. Sohn, J. I.; Choi, S. S.; Morris, S. M.; Bendall, J. S.; Coles, H. J.; Hong, W. K.; Jo, G.; Lee, T.; Welland, M. E. Novel Nonvolatile Memory with Multibit Storage Based on a ZnO Nanowire Transistor. *Nano Lett.* **2010**, *10*, 4316–4320.
25. Liu, H.; Sun, J.; Jiang, J.; Tang, Q.; Wan, Q. Transparent SnO_2 Nanowire Electric-Double-Layer Transistors with Different Antimony Doping Levels. *IEEE Electron Device Lett.* **2011**, *32*, 315–317.
26. Shen, G.; Liang, B.; Wang, X.; Huang, H.; Chen, D.; Wang, Z. L. Ultrathin In_2O_3 Nanowire Mats for Transparent Thin-Film Transistor Applications. *ACS Nano* **2011**, *5*, 6148–6155.
27. Liao, L.; Zhang, Z.; Yan, B.; Zheng, Z.; Bao, Q. L.; Wu, T.; Li, C. M.; Shen, Z. X.; Zhang, J. X.; Gong, H.; Li, J. C.; Yu, T. Multifunctional CuO Nanowire Devices: p-Type Field Effect Transistors and CO Gas Sensors. *Nanotechnology* **2009**, *20*, No. 085203.
28. Liu, H.; Reccius, C. H.; Craighead, H. G. Single Electrospun Regioregular Poly(3-hexylthiphene) Nanofiber Field-Effect Transistor. *Appl. Phys. Lett.* **2005**, *87*, No. 253106.
29. Min, S.-Y.; Kim, T.-S.; Kim, B. J.; Cho, H.; Noh, Y.-Y.; Yang, H.; Cho, J. H.; Lee, T.-W. Large-Scale Organic Nanowire Lithography and Electronics. *Nat. Commun.* **2013**, *4*, No. 1773.
30. Wu, H.; Lin, D.; Zhang, R.; Pan, W. ZnO Nanofiber Field-Effect Transistor Assembled by Electrospinning. *J. Am. Ceram. Soc.* **2008**, *91*, 656–659.
31. Wu, H.; Lin, D.; Pan, W. Fabrication, Assembly and Electrical Characterization of CuO Nanofibers. *Appl. Phys. Lett.* **2006**, *89*, No. 133125.
32. Omata, T.; Ueda, N.; Ueda, K. New Ultraviolet-Transport Electroconductive Oxide, $ZnGa_2O_4$ Spinel. *Appl. Phys. Lett.* **1994**, *64*, 1077–1078.
33. Kim, I. D.; Rothschild, A.; Lee, B. H.; Kim, D. Y.; Jo, S. M.; Tuller, H. L. Ultra-sensitive Chemiresistors Based on Elecrospun TiO_2 Nanofibers. *Nano Lett.* **2006**, *6*, 2009–2013.
34. Choi, S. H.; Hwang, D. S.; Kim, D. Y.; Kervella, Y.; Maldivi, P.; Jang, S. Y.; Demadrille, R.; Kim, I. D. Amorphous Zinc Stannate(Zn_2SnO_4) Nanofibers Networks as Photoelectrodes for Organic Dye-Sensitized Solar Cells. *Adv. Funct. Mater.* **2013**, *23*, 3146–3155.
35. Kim, D. H.; Cho, N. G.; Han, S. H.; Kim, H. G.; Kim, I. D. Thickness Dependence of Gate Dielectric and Active Semiconducting $InGaZnO_4$ Thin Film Transistor Fabricated on Plastic Substrates. *Electrochem. Solid-State Lett.* **2008**, *11*, H317–H319.
36. Lee, S. Y.; Park, B. O. Electrical and Optical Properties of In_2O_3-ZnO Thin Films Prepared by Sol-Gel Method. *Thin Solid Films* **2005**, *484*, 184–187.
37. Choi, S. H.; Hyun, T. S.; Lee, H. J.; Jang, S. Y.; Oh, S. G.; Kim, I. D. Facile Synthesis of Highly Conductive Platinum Nanofiber Mats as Conducting Core for High Rate Redox Supercapacitor. *Electrochem. Solid-State Lett.* **2010**, *13*, A65–A68.
38. Shieh, M. S.; Sang, J. Y.; Chen, C. Y.; Wang, S. D.; Lei, T. F. Electrical Characteristics and Reliability of Multi-Channel Polycrystalline Silicon Thin-Film Transistors. *Jap. J. Appl. Phys.* **2006**, *45*, 3159–3164.
39. Cho, N. G.; Kim, D. H.; Kim, H. G.; Hong, J. M.; Kim, I. D. Zinc Oxide Thin Film Transistor Using MgO-$Bi_{1.5}Zn_{1.0}Nb_{1.5}O_7$ Composite Gate Insulator on Glass Substrate. *Thin Solid Films* **2010**, *518*, 2843–2846.
40. Nomura, K.; Ohta, H.; Takagi, A.; Kamiya, T.; Hirano, M.; Hosono, H. Room-Temperature Fabrication of Transparent Flexible Thin-Film Transistors Using Amorphous Oxide Semiconductors. *Nature* **2004**, *432*, 488–492.